

A Developed Algorithm for Automating the Multiple Bands Multiple Endmember Selection of Hyperion data Applied on Central of Cairo, Egypt

Waleed Effat^{1*} Osman Hegazy² Mohamed NourEldien²

1. Esri Northeast Africa, 4 El-Mathaf El-Zerai, Agouza, PO 12311, Giza, Egypt
2. Faculty of Computers and Information, Cairo University, PO Box 12613, Giza, Egypt

* E-mail of the corresponding author: waleed.effat@gmail.com

Abstract

This study attempts to provide an answer regarding the utility of Hyperion imagery in mapping urban settings in developed countries. The authors present a novel method for extracting quantitative land cover information at the sub-pixel level from hyperspectral or Hyperion imagery. The proposed method is based on the multiple endmember spectral mixture (MESMA) proposed by Roberts et al. (1998b), but extends it to handle the high-dimensional pixels characterizing hyperspectral images. The proposed method utilizes a multiband multiple endmember spectral mixture analysis (Multiband MESMA) model that allows for both spectral bands and endmembers to vary on a per-pixel basis across a hyperspectral image. The goal is to select an optimal subset of spectral bands that maximizes spectral separability among a candidate set of endmembers for a given pixel, and accordingly to minimize spectral confusion among modeled endmembers and increase the accuracy and physical representativeness of derived fractions for that pixel.

The authors develop a tool to automate this method and test its utility in a case study using a Hyperion image of Central Cairo, Egypt. The EO-1 Hyperion hyperspectral sensor is the only source of hyperspectral data currently available for Cairo, unlike cities in Europe and North America, where multiple sources of such data generally exist. The study scene represents a very heterogeneous landscape and has an ecological footprint of a complex range of interrelated socioeconomic, environmental and urban dynamics. The results of this study show that Hyperion data, with its rich spectral information, can help address some of the limitations in automated mapping that are reported by previous studies. For this, proper bands and endmembers are selected and used within a multiple endmember, with a multiple-band SMA process to determine the best Root Mean Square Error (RMSE) and abundance percentages. This results in a better mapping of land cover extricated from hyperspectral imagery (Hyperion).

Keywords: Spectral Mixture Analysis, Hyperspectral Data, Hyperion Data, Cairo, Egypt

1. Introduction

Urban remote sensing is one of the most affordable means of obtaining information and enriching our understanding of the processes and dynamics of cities, especially in the context of developing countries where conventional methods of survey are costly. Ongoing research themes focus on three main areas of application (Weng et al. 2012). The first application area is the mapping and delineation of urban land cover and land use. The increasingly diverse nature and commercial availability of sensor systems and imagery products for urban areas have enriched available opportunities for mapping and monitoring changes in urban landscapes at various scales (Fugate et al. 2010; NRC 2007). Recent research features have increased the use of hyperspectral imagery, LiDAR sensor technologies, and fused imagery to facilitate more accurate measurements of land cover or land use within the urban scenes (Chen and Vierling 2006; Franke et al. 2009; Guo et al. 2011; Herold et al. 2008; Roberts et al. 2012).

The second application area is the analysis of patterns and biophysical properties of urban landscapes. The goal is to ingest the information extracted from remote observations into the scientific analyses of diverse urban phenomena in support of decision making and wise management of urban resources. Although specific goals of the studies differ, most attempt to develop quantitative models that make use of remotely sensed measures to describe a certain aspect of urban dynamics. Examples include urban growth, response of urban ecosystems to climate change, and empirical models of demographic and socioeconomic processes (Mesev 2003; Rashed and Juergens 2010; Weng 2008; Weng

and Quattrochi 2007).

The third application area dominating urban remote-sensing research is the development of image-processing algorithms and techniques that improve the practical use of urban imagery. In a recent survey Weng et al. (2012) classified the methods and techniques proposed in urban remote-sensing literature into eight major approaches: pixel-based classification, subpixel based methods, object-oriented algorithms, artificial neural networks, data or image fusion, expert systems, and contextual classification methods. None of these approaches are superior to the others, and the utility of each approach depends largely on the goals of the study, data used, and characteristic and context of the urban scene to which the approach is applied.

The research presented in this paper falls mainly under the third application area—the development of image-processing algorithms and techniques—but also addresses the other two areas. We present a new method developed for extracting quantitative land cover information at the sub-pixel level from hyperspectral imagery. The proposed method is based on the multiple endmember spectral mixture (MESMA) model originally proposed by Roberts et al. (1998b), but we extend it to handle the high-dimensional pixels characterizing hyperspectral images. It utilizes a multiband multiple endmember spectral mixture analysis (Multiband MESMA) model that allows for both spectral bands and endmembers to vary on a per-pixel basis across a hyperspectral image. The goal is to select an optimal subset of spectral bands that maximizes spectral separability among a candidate set of endmembers for a given pixel, and then accordingly minimize spectral confusion among the modeled endmembers and increase the accuracy and physical representativeness of derived fractions for that pixel.

In this paper, we develop a tool to automate this method and test its utility in a case study using a Hyperion image of Central Cairo, Egypt. The EO-1 Hyperion hyperspectral sensor is the only source of hyperspectral data that is currently available for Cairo, unlike cities in Europe and North America where multiple sources of such data generally exist. The study scene represents an extremely heterogeneous landscape that represents an ecological footprint of a complex range of interrelated socioeconomic, environmental, and urban dynamics. As such, the study site offers an ideal context to test the utility of the proposed method not only in terms of its effectiveness but also as to whether Hyperion-derived fractions can relate to urban biophysical processes and other dynamics better than fractions derived from multispectral images.

In the following sections, we first provide a review of the use of Hyperion imagery in urban studies, and how the techniques of spectral unmixing have been applied to Hyperion and other types of hyperspectral images. We then present our methodology and describe the study area of our case study in Central Cairo. Finally, we present our results and discuss the findings, and conclude with plans for future work.

2. Background

2.1. Hyperion Sensor and its Urban Applications

Recent literature on urban remote sensing shows a trend toward examining the utility of imaging spectroscopy and hyperspectral imagery in analyzing spatial and spectral patterns of urban features (Chen et al. 2003; Chen and Vierling 2006; Franke et al. 2009; Fugate et al. 2010; Herold et al. 2008; Roberts et al. 2012; Weng 2012). The bulk of published research in this area is concerned with the measurement, analysis, and interpretation of spectra acquired from specific objects in a given urban scene. The premise of this work is that “the application of remote-sensing technology for mapping the urban environment requires specific attention to the spectral dimension” and that “hyperspectral data offers capabilities of improved spectral and spatial urban mapping capabilities” (Herold et al. 2004, pp. 304).

NASA’s EO-1 Hyperion sensor has been designed as a test bed instrument to demonstrate hyperspectral imaging from space (Pearlman et al. 2000). It has a 7.5-km swath width, a 30-m ground resolution, and 220 unique spectral channels with 10-nm spectral resolution covering a spectrum from 0.357 to 2.576 μm (Beck 2003). Only 198 bands are calibrated because of the sensor’s low responsiveness in some channels, of which there are 196 unique channels because of an overlap between the VNIR and SWIR focal planes (Beck 2003; Pearlman et al. 2000). The bands that are not calibrated are set to zero in those channels.

With the launch of the Hyperion sensor in late 2000, one expected to see several applications geared to test the utility of satellite-based hyperspectral mapping capability in cities of the developing world. Surprisingly, to date, more than a decade after its launch, there is no or little published research that examines the utility of Hyperion sensor in urban

settings in general, and in developing countries in particular. This lack of progress may be attributed to two main reasons.

First, majority of urban applications of hyperspectral data have dealt with urban settings in cities in developed countries (e.g., Franke et al. 2009; Herold et al. 2003), where airborne hyperspectral sensors such as AVIRIS and HyMap are available and provide better coverage and better quality data than Hyperion. In the context of cities in developing countries, the high cost and limited coverage of airborne sensors, coupled sometimes with flying restrictions imposed by authorities, continue to represent a barrier to using data from these sensors (Plaza et al. 2009). At the same time, it is widely assumed by many in developing countries that higher spatial resolution data are required for urban-mapping applications. Therefore, the application of urban remote sensing in developing countries continues to rely, to a large extent, on space platforms of multispectral bands with high and medium spatial resolutions.

Second, there is a need for new methods and techniques that are capable of handling this high-dimensional dataset to measure and retrieve parameters describing urban land cover. With a ground spatial resolution of 30 m, each pixel in a Hyperion image is expected to cover a diverse set of urban materials and land cover interwoven with each other. Mathematical algorithms need to be developed and tested to tackle both the problem of mixed pixels and identification of optimal spectral bands that maximize spectral separability for urban classification and mapping.

With these two challenges in mind, this study is among the first applications that attempt to provide an answer to the utility of Hyperion imagery in mapping urban settings of developed countries. We hope that the methodology we are presenting here helps provide an empirical base for a new framework for the urban application of Hyperion imagery in developing cities.

2.2. *Spectral Unmixing in Hyperspectral Imagery of Urban Areas*

Urban hyperspectral datasets provide continuous spectral coverage of features over narrowed spectral bands, and as such, they pose different challenges from an image-processing perspective. The progress in hyperspectral remote sensing has been fueled by the development in hyperspectral analysis methods and the accumulation of detailed spectral libraries acquired in the field or in the laboratory. Several machine-learning and image-processing techniques have been developed and applied to hyperspectral data including spectral matching, spectral unmixing, wavelet analysis, spectral angle mapping, and segmentation (Campbell and Wynne 2011). Of these techniques, spectral mixture analysis is one of the most popular methods used in the context of both urban remote sensing and the analysis of hyperspectral images (Adams et al. 1993; Adams et al. 1986; Adams et al. 1995; Franke et al. 2009; Rashed et al. 2003; Roberts et al. 1998a; Small 2001; Weng 2012; Wu and Murray 2003).

The spectral mixture analysis (SMA) technique is a process for solving endmember fractions, assuming that the spectrum measured for each pixel represents a linear combination of endmember spectra (Adams et al. 1993; Adams et al. 1986; Adams et al. 1995). Endmembers refer to the spectral response of land cover materials with uniform properties present in a scene. Standard SMA models implement an invariable set of endmembers to model the spectra in all the pixels within an image. These models usually fail to account for the fact that, because of the diversity of urban materials, the number and type of components within the field of view are variable (Rashed et al. 2003). If a pixel is modeled by fewer endmembers than required, the unmodeled portion of the pixel spectrum will be partitioned into the resultant fractions, thus increasing the model error for that pixel (Roberts et al., 1998b). Similarly, the use of numerous endmembers to unmix the pixel spectrum will result in fraction errors due to spectral confusion among these endmembers.

To address the limitations of standard SMA models, Roberts et al. (1998b) proposed a modified method called MESMA. The MESMA model is based on the concept that although the spectra in any individual pixel can be modeled with relatively few endmembers, the number and type of endmembers are variable across an image. In this sense, MESMA can be described as a modified linear SMA approach in which many simple SMA models are first calculated for each pixel in the image. The objective is then to choose, for every pixel in the image, which model amongst the candidate models provides the best fit to the pixel spectra while producing physically reasonable fractions (Rashed et al. 2003).

A number of studies have examined the application of MESMA in urban settings using multispectral images (e.g., Powell and Roberts 2008; Powell et al. 2007; Rashed 2008; Rashed et al. 2003). Reported results show superior performance over standard SMA models when applied to the same urban settings (Rashed 2008). A few studies

recently have applied MESMA to the hyperspectral mapping of urban areas. However, because of the high dimensionality of hyperspectral data, some proposed modifications to the original MESMA seem to be necessary. Franke et al. (2009), for example, proposed a hierarchical MESMA that was applied to airborne HyMap data to analyze the urban environment of Bonn in Germany. In their hierarchical structure of MESMA, two-, three-, or four-endmember models were uniquely tailored to four levels of urban complexity. Results with appropriate classification accuracies from one level were then used as spatial constraints for the next level for improving mapping accuracy. Another variation of MESMA in the context of hyperspectral image was proposed by Somers et al. (2009). They proposed a nonlinear MESMA (nMESMA) for mapping tree covers in a commercial area in South Africa. The nMESMA model accounts for the effect of nonlinearity within the mixed model by simulating the effects of a series of endmember models and evaluating the resultant root mean square error (RMSE) values. The endmembers of the model that produces the minimal RMSE value and is physically meaningful are then used in the spectral-unmixing algorithm.

Both the hierarchical MESMA and nMESMA approaches focus mainly on enhancing the performance of MESMA by improving the endmember selection associated with the within-class spectral variability of a pixel. In the context of multispectral imagery, where a limited number of bands exist for any given pixel, such focus seems to be quite valid and important. However, in the context of hyperspectral imagery, where so many spectral bands exist for any given pixel, attention is required to the optimal number of bands that can be used in the MESMA modeling because these bands are critical in calculating the RMSE values. In this study, we propose a methodology that balances both sides of the equation, the endmembers and modeled spectral bands, by allowing both endmembers and modeled bands to vary on a pixel by pixel basis throughout the imagery.

3. Study Site and Methods

3.1. Study Area

The proposed methodology was applied and tested on a study site in Cairo, Egypt. The chosen study area was located in the central area of the Greater Cairo region (Figure (1)) at the interface of three main administrative boundaries: the Governorate of Cairo (located on the east bank of the Nile River), Governorate of Giza (located on the west bank of the river), and southern area of the Governorate of Qalyubia. The study site covers an area of 59.29 km² and includes a variety of land uses associated with a complex mix of land cover.

In general, we selected this site because it represents a blueprint for a range of challenges typically faced by remote-sensing analysts when applying multispectral imagery to urban analyses in developing countries, and in Cairo in particular. For example, previous studies have reported challenges associated with mixed pixels in the context of multispectral image applications in Cairo (Fugate 2003; Rashed et al. 2001; Sutton and Fahmi 2001; Weeks et al. 2004). The problem of the mixed pixel is induced by a broad range of land cover types that are continuously changing over an extended agglomeration area comprising very dense built-up areas and extending all the way to farmland and rural areas in the northeast part of the imagery. Along this continuum of land cover, there is a great deal of mixed land use in which commercial, residential, recreational, and industrial uses are difficult to separate from one another. As reported in previous studies, this mixed use of land poses many great challenges and yields less useful results when applying traditional per-pixel supervised or unsupervised image-classification techniques because of the mixed-pixel problem (Rashed et al. 2001; Weeks et al. 2004).

Furthermore, the presence of spectral-like artifacts adds difficulty to interpreting spectral signals using multispectral imagery because of the limited spectral information inherent in such imagery. For example, the dense arrangement of tall buildings in the area of the study generates shade that is spectrally similar to the spectral response of the large water body presented by the Nile River when using such data as Landsat TM, IRS, or SPOT. Similarly, the “dirt” materials used to cover the roofs of buildings in rural, slum, and less affluent urban areas yield a similar spectral response to bare soil (Rashed et al. 2005). Such issues impose a greater limitation on the usefulness of multispectral images in terms of how retrieved spectral singles can be interpreted, which in turn hinders the possibility for automated mapping. As mentioned earlier, one of the objectives of this study is to examine the degree to which Hyperion data, with its rich spectral information, can help address some of these limitations and yield better classification results.

3.2. Image Acquisition and Initial Preparation

The Hyperion image used in this study was acquired in April 2002. The image used presents a 7.7×7.7 km subset of the original 7.7×42 km Hyperion scene acquired for a study covering a spectral range from 356 to 2577 (nm) over 242 spectral bands, 70 of which were VNIR bands (356–1058 nm), and the rest of which were SWIR bands (852–2577 nm). Only the 196 calibrated bands (bands 8–57 for the VNIR, and bands 77–224 for the SWIR) were considered in this study. The 10-nm bandwidth of the spectral channels was at a spectral resolution of 30 m. The original scene was already acquired a “Level 1B,” which is already radiometrically corrected. The Hyperion Level 1A dataset was generated from the Level 0 dataset through several processing steps including smear correction, echo correction, background removal, radiometric correction, repair of bad pixels, and checking image quality (Pignatti et al. 2009).

To prepare the image for analysis, we performed a number of preprocessing operations following the procedure described in Beck (2003). The first step in this procedure was to convert Hyperion Level 1-B data into absolute radiance by using the Band Math function in ENVI software. The second step was to correct the radiance data for atmospheric effects to create reflectance values for the imagery. For this step, we used the fast line-of-sight atmospheric analysis of the spectral hypercube (FLAASH) algorithm in ENVI software. The outcome of this second step was further examined and 38 resulting bands were identified as “bad bands.” This screening left us with only 158 bands (from 0.4268 to 2.3352 μ meter), which we used in all subsequent analyses performed in this study.

The final pre-processing step applied to the imagery was geometric correction. The Hyperion image was georeferenced using a geometrically corrected QuickBird high-resolution image (0.6 m) of the same study sites, along with some additional ground control points measured by GPS. The number of ground control points was 20. The resultant RMSE after the georeferencing process was 3.8 m.

3.3. Multiband MESMA Model

The rest of this section is devoted to presenting the Multiband MESMA model that was developed and tested in the context of this study. In developing the Multiband MESMA model we were mindful of two main challenges that we were facing in utilizing the Hyperion image of Cairo: (1) how to identify an optimal set of endmembers that represent the land cover classes of interest the closest, and (2) for each unique combination of endmembers, how to extract from the Hyperion image, a subset of optimal bands that offers maximum separability among the endmembers.

Figure (2) illustrates the main elements of the Multiband MESMA approach. As shown in the figure, the approach comprises five main steps. The first two steps focus on selecting the optimal combination of endmembers for a given pixel. The best combination of endmembers is determined on the basis of the abundance percentages of endmember fractions that are physically meaningful (i.e., between 0% to 100%) and provide minimum RMSE values. The third step is focused on selecting an optimal subset of bands for the endmember combination. The rest of the steps are focused on executing a spectral mixture analysis and evaluating the results on a pixel-by-pixel basis. An automated algorithm was developed to run this procedure on a pixel-by-pixel basis, the details of which are discussed below.

3.4. Selections of Endmembers

It has frequently been said that one of the major challenges in spectral mixture analysis applications is the selection of an appropriate set of candidate endmembers (Franke et al. 2009; Milton 1999; Roberts et al. 1998b; Rogge et al. 2007; Tompkins et al. 1997). This challenge is particularly acute in the context of hyperspectral imagery because the higher spectral resolution of these images translates into a broader range of possible endmembers that can be used in the spectral unmixing.

There are two types of endmembers: image endmembers and reference endmembers. We utilized the former in this research because of the absence of a field or laboratory spectral library compiled for the study area. An image endmember is identified as the spectral response of a pixel or average spectral response of a group of pixels that may hold spectra that represent the reflectance of one homogeneous feature known to be present on the ground surface. It is referred to as image endmember because it is selected directly from the image.

Guided by the previous studies that were carried out in Cairo (Fugate 2003; Rashed et al. 2001; Rashed et al. 2005; Weeks et al. 2004), in addition to the authors’ knowledge of the area, we selected a set of endmembers that correspond to broader land cover types (rather than specific materials) known to be present on the study scene. These

included water bodies (mainly the Nile River), shadows (of buildings and trees), bare soil (sport yards, dirt in vacant land and farmlands), impervious surfaces (building roofs and roads), and vegetation (croplands and parks) (see Table 1).

The selection of image endmembers was based on the purity pixel index (PPI) algorithm, a method that was originally developed by Boardman et al. (1995) and is currently implemented in ENVI software. The PPI method allocates a score to each pixel on the basis of the number of times it is found to occupy a near-vertex position in the repeated projections of the n-dimensional data on a randomly oriented vector passing through the mean of a data cloud. The resulting score helps identify image endmembers because those pixels that hold pure spectra will be found repeatedly at the extremes of the data distribution. When the image includes a high number of bands as in the case of Hyperion data, the PPI algorithm would typically run on the result of a minimum noise fraction (MNF) transform first applied to this image to exclude the noise bands. We did not perform MNF transformation in this study as we had already excluded these noise bands in the pre-processing stage and reduced the number of usable bands to only 158 bands.

The process of endmembers selection using PPI can be summarized as follows:

1- Run the PPI on ENVI software using 10,000 as the Number of Iterations, and 5 as the Threshold Factor. The “Number of Iterations” parameter refers to the number of n-dimensional projections the PPI algorithm will perform. The “Threshold Factor” parameter is the maximum number of vertexes or extreme pixels that will be considered pure in a given PPI iteration; the value of five means that the first five pixels found on a given node of the pixel cloud will be assigned to a PPI score of one. If they are found on a second iteration, then they are assigned two as a score and so on. Note that there is no rule of thumb as to how many iterations the PPI algorithm needs to run. The number depends on how many bands an image has, speed of the computer processor, and available memory.

Once run, the PPI algorithm will yield a “PPI image” showing the number and locations of pure pixels, and a “PPI plot” showing the number of iterations performed on the X-axis versus number of pure pixels found on the Y-axis. The curve shown in the plot can be used to determine whether the number of selected iterations is sufficient. When the curve is flat (i.e., parallel to the X-axis), it implies that the number of iterations selected for the PPI algorithm is sufficient. When it is not, that is an indication that the PPI algorithm should be executed for more number of iterations. The PPI image shows the pixels which were identified as pure by the PPI. The value associated with each pixel refers to the number of times a pixel is identified as pure. For example if a pixel value is 130, this means that the pixel has been found as extreme 130 times out of 10,000 iterations run by the PPI algorithm.

2- Select from the resultant PPI image a subset of pixels that can later be used to derive endmembers. To do this, we first need to identify a cut-off PPI value for the pixels that we want to further consider in our analysis. The cut-off value needs to be large enough to ensure that the pixel was not identified as extreme by chance and that it is representative of an actual endmember. In this study, we selected a cut-off value of 10, which means that a pixel needs to be identified as extreme more than 10 times for it to be considered in the image endmember selection. The selection of this cut-off value was somewhat arbitrary to avoid “noise” pixels that are located on the edge of the image.

3- Look at the results from Step 2 using the “N-Dimensional Visualizer” tool in ENVI software to identify clusters of pure pixels and derive the final set of endmember candidates from these clusters. Identification of clusters requires a good knowledge of the study scene and an iterative process of selection or validation until the clusters of candidate endmembers are identified in the n-dimensional space.

4- Calculate the average spectral response of final selected clusters to derive the spectral profiles of candidate endmembers. Figure (3) shows the final set of candidate endmembers we derived for this study following the above procedure.

3.5. Endmember Combination and Selection of Optimal Bands

As we highlighted earlier, the basic idea of the MESMA approach is that endmembers can vary per pixel. In other words, the unmixing algorithm does not need to use the 10 candidate image endmembers we have identified to resolve the physical abundance of land cover. In most cases, a combination of only two to four endmembers is sufficient for a given pixel, especially when these endmembers represent broad land cover categories (as opposite to specific land materials), as is the case in this study.

The unmixing algorithm developed in this study extends the MESMA method beyond the ability to vary the combination of endmembers to the selection of an optimal subset of candidate image bands on a per-pixel basis.

Our approach is an extension of Roberts et al. (1998b) approach in MESMA. We adopted the same process however we have added the selection of optimal bands.

The idea is simple; for a given pixel in the hyperspectral bands, not all the 158 “good bands” of the Hyperion image are needed to perform spectral mixture analysis. Rather, once we are able to identify a subset of endmembers combination for a given pixel, we only need those bands that maximize the spectral separability between the endmembers selected to perform the spectral unmixing at this pixel. Spectral separability is defined in the context of this study as the distance or difference between the reflectance values of two or more endmembers at a given band (Figure (4)). The higher the spectral separability distance between endmembers at a given band, the better performance of the unmixing algorithm and hence the better fraction results the algorithm is expected to produce at this band.

We developed an add-on tool for ENVI software that enables the user to perform this process in an automated way. The algorithm behind this tool, called `doCombinations_pro`, allows the user to generate a list of all possible combinations for endmembers for a given pixel, and then calculate the spectral separability distance for each combination. The final endmember combination selected for a given pixel is the one that maximizes the spectral separability distance among these endmembers, while producing the lowest RMSE values and physically meaningful endmember fraction results (i.e., fraction values between 0% and 100%).

Figure (5) shows the developed widget used to account for all possible endmember combinations on a per pixel basis. It allows the user to enter the total number of endmembers (10 in the case of this study) and lower and upper limits of a single combination (combination threshold). The widget will then automatically produce all possible combinations among these endmembers with a numeric label identifier for each endmember. In this study, we set the lower and upper limits of any single endmember combination to two and four, respectively, on the basis of the previous studies by Robert et al. (1998b) and Rashed et al. (2003), which proposes that any given pixel of 30-m resolution in urban areas is not likely to possess more than four endmembers within its spatial extent. Widget output is a text file (also shown in Figure 5) that contains the total number of available combinations of the provided endmembers, in addition to listing of each combination and the endmembers used in that combination.

Once the list of all possible endmember combinations is generated, it is inputted into another developed ENVI/IDL algorithm, called `getBands_pro`, to select the optimal subset of spectral bands for each combination based on the spectral separability distance. The formula used in this algorithm is as follows: for a single combination of n number of endmembers, generate a Band List array where the band of wavelength λ is included in the Band List only if it meets the following condition for any endmembers i and j in the combination:

$$R_{\text{diff}} = |R_i - R_j| \geq \rho, \quad (1)$$

where

R_i is the reflectance value of i th endmember at wavelength λ in each single combination of n endmembers;

R_j is the reflectance value of j th endmember at wavelength of λ in each single combination of n endmembers;

R_{diff} is the difference between the reflectance value of i th endmember and the reflectance value of j th endmember at wavelength of λ in each single combination of n endmembers; and

ρ is the minimum separability distance value specified by the user (8.5% if not specified)

The `getbands_pro` algorithm accepts a default minimum separability distance of 8.5%, i.e., the minimum difference in the spectral reflectance values of any two endmembers in a given band needs to be 8.5% or more for using this particular image band in the spectral unmixing. However, the user has the option to select other minimum separability distance as deemed appropriate for the analysis and context of a study. The output of the `getbands_pro` algorithm can be displayed on the IDL console screen, or produced in a text file for further processing. The output shows the number and types of endmembers used for a given combination, followed by a list of bands, each of which is labeled by a unique combination ID that meets the condition of having a separability distance equal or greater than the specified distance for that particular combination. We chose to start the combination ID at number 1000 and it continues sequentially. The output text file contains these combinations organized in rows, where each row represents a single combination, as shown in Figure (6). The selected bands are represented by their sequential order

number in the original Hyperion image. The order is a zero-based order, which means that the first and second bands have an order of zero and one, respectively.

3.6. Multiband Multiple Endmember Spectral Mixture Analysis

The output text file of `getbands_pro` is inputted into another IDL-developed algorithm called `dowork_pro`, which repeatedly applies a constrained linear spectral unmixing algorithm to the hyperspectral image using the combinations listed in the text file. Each run of the unmixing algorithm produces a multiband image resulting from a single combination, in which the abundance fractions of each endmember in that combination are represented as a single band. The resultant multiband image includes an additional root mean square error (RMSE) band, where the value in each pixel represents the RMSE that resulted from solving the unmixing algorithm using the endmembers at this particular pixel.

The `dowork_pro` algorithm assesses each combination on a pixel-by-pixel basis, and rejects those combinations that violate the following conditions for both abundance percentages and RMS value.

$$1.05 > \sum_e^n f_e s_e > 0.95 \quad (2)$$

and

$$RMSE \leq RMSE_{max} \quad (3)$$

where

f_e is a fraction or abundance value from 0 to 1 of the endmember e contributing to the spectral response of the pixel, n is the total number of endmembers within a certain combination, and RMSE is the root mean square error per pixel that represents the difference between the observed mixed spectrum and calculated mixed spectrum. $RMSE_{max}$ is the maximum allowable RMSE values and it is an input to the algorithm. The default value of $RMSE_{max}$ is 0.025.

As indicated in Equation (2), the algorithm restricts the sum of fraction values produced by a given model in a given value within the range 0.95–1.05, assuming a margin error of 5%. However, the program also gives the user the option to change these margin error values as required.

Models that represent various combinations of endmembers are screened on a pixel-by-pixel basis on the basis of the above conditions. A model is selected for a pixel if it meets the conditions stated in Equations (1) and (2) and produces the lowest RMSE value. In such a case, the pixel will be assigned to a value that represents the ID of the selected model. The output of running this algorithm across all pixels is a model suitability raster image, in which pixels values represent the ID of the most suitable model (endmember combination) selected for each pixel. In addition, two other raster images are created along with the model suitability image. The first one is a raster image in which each pixel value represents the sum of the fraction values that was produced from running the model that was deemed suitable for the pixel named Abundance Value Raster. The second one is a raster image in which each pixel value represents the RMSE value from running the corresponding model (see Figure (7)). The latter two images were used to ensure that each model with a suitable raster produces an acceptable RMSE and the sum of the fraction values.

3.7. Accuracy Assessment

An accuracy assessment of the results was performed by superimposing the Abundance Value Raster that has the same spatial resolution as the original Hyperion data that is 30 m, and the classified QuickBird image, where each pixel of Hyperion data contains 2500 (50×50) pixels of QuickBird image. The QuickBird image was classified into 10 classes (land covers) matching the 10 endmembers selected for the Hyperion image. The classified QuickBird image was considered as guidance for assessing the correctness of the models. A random sampling algorithm was developed to select 40 regions of interest (ROIs) in the Hyperion data. Each ROI is located within one pixel of the Hyperion image. To calculate the QuickBird fractions we looped through each of the ROI regions and located the corresponding 2500 QuickBird classified pixels, and these 2500 pixels were examined against each class to determine the number of pixels allocated for this class. Then the fractions were calculated.

The abundance fractions within this Hyperion pixel were then regressed against the endmember (materials) percentages within the corresponding 2500 QuickBird pixels. The random algorithm inputs are the lower left and upper right coordinates of the area of study. An IDL function is applied to generate 40 ROIs within the area of the study by applying the following equation:

$$x_i = |Randomn| * (x_{ur} - x_{ll}) \quad (4)$$

$$y_i = |Randomn| * (y_{ur} - y_{ll}) \quad (5)$$

Where x_i and y_i are the coordinates of a random point i ,

x_{ur} and y_{ur} are the coordinates of the upper right corner of the area of the study,

x_{ll} and y_{ll} are the coordinates of the lower left corner of the area of the study.

The RANDOMN function returns a normally distributed, floating-point, pseudo-random number with a mean of zero and a standard deviation of one. The algorithm repeats the RANDOMN function many times to create a number of random points. By default, the number of ROIs is 40; however, this number can be changed if needed. The factor that determines the ROIs number is the dimensions of the area of the study, as shown in Figure (8).

Finally, a regression line is created between the Hyperion fractions and QuickBird fractions for each endmember to assess the accuracy of the model.

4. Results and Discussion

4.1. Results of Bands Selection

The number of output endmember combinations resulting from doCombinations_pro (see Figure 5) is 375 combination models with different bands that give the desired separability distance for each combination. Table 2 provides a summary of the output combinations and endmembers for each combination.

The maximum number of used bands is 46, while the minimum number of used bands is six. The separability distance is the only factor that controls the number of bands used. Some combinations can be manually eliminated before applying spectral unmixing. This elimination may be needed when the combination of certain endmembers does not make sense, where the existence of certain endmembers in the same combination is impossible in reality e.g. the combinations that include Deep_Nile endmember (Deep River) and Building_Shadow endmembers or Sports_Yard are eliminated. The output text file is used to run the SMA on each combination. After elimination, the combination is reduced to be 369 combinations.

4.2. Multiband Multiple Endmember Spectral Mixture Analysis

For each combination from the 369 available combinations, three raster images are created: 1) a suitability model raster, 2) resulting abundance raster, and 3) resulting RMS raster. The suitability model raster contains pixels with values of the best models (combination IDs) that achieve maximum separability distance and proper RMSE values. The other two raster are created for reference as their pixels values contain the correspondence sum of the abundances and RMSE values, respectively.

Within the area of study, 74 of the 369 models are fitted and give the proper sum of the abundance fractions and RMSE. The average of the sum of the abundances fractions within the area of study using the 74 models is 95.34%, and the average RMSE is 0.021% of the pixels. Some pixels could not be mapped to certain models; these pixels are represented in the three raster images with a value of NoData. We instigated these areas and found that increasing the allowable RMSE from 0.025 to 0.035 resolved the unmapped pixels, and all the models (combinations) can be successfully applied. However, this increase in the RMSE values resulted in an increase in the mean RMSE percentage to 0.024% and a decrease in of the average of sum of the abundances percentage to 93.1%.

The suitability raster image within the area of study is shown in Figure (9).

4.3. Results Discussion

To illustrate the output of the text file content in Figure (6), we took one record (row), i.e., model number 1103, of this file as an example. The record contains the combination ID, endmembers list, and selected bands list. Table 3 illustrates the selected record content.

The endmember combination number 1103 was plotted in one graph to check that the listed bands are ones that have separability distances greater than or equal 8.5% of the reflectance. Each band is presented by locating its wavelength value on the graph. The wavelengths of the bands are available in the ENVI Band List widget. Table 4 lists the wavelength for each band listed in Table 3, and are plotted in a graph as shown in Figure (10).

It is worth mentioning that we opted the 8.5% as a default separability distance percentage as it gives 6 suitable bands as a minimum. Using more than 8.5% in our case study may result in choosing less than 6 bands.

The listed bands in Table 4 are the bands that provide a separability distance greater than or equal 8.5% from the reflectance. Figure (10) shows these separability distances in the spectral graphs of the three listed endmembers.

A close-up image of the Suitability Model Raster is presented in Figure (11) to compare the fitting of the raster model with the QuickBird image.

The green field that appeared in the QuickBird image is represented by Model 1020, while the built-up area is represented by Model 1030. Model 1020 contains two endmembers: BareSoil1_Dirt and UrbanGreen1_Grass. This combination almost represents the green field in the QuickBird image, while Model 1030 also contains two endmembers, which are Built_HighAlbedo_Concerte and Building Shadow. The built-up area in the QuickBird image is almost composed of these two endmembers.

4.4. Accuracy Assessment

After applying the sampling process, a regression line is created between the Hyperion fractions and QuickBird fractions to assess the accuracy of the model. Table 5 illustrates the slope, interception, and R^2 values for each endmember.

The average of R^2 is 0.7725, which means that the models are averagely fitting around 77% of the data. However, this regression value is mainly dependent on the accuracy of the superimposing process of both the Hyperion data and QuickBird data. Some discrepancies are noted, and this occurs for two reasons: 1) the resolution mismatch between the Hyperion data and QuickBird data, and 2) the accuracy of the ground control points obtained and resulting RMSE values with the rectification process.

Figure (12) illustrate the regression results between the Hyperion fractions and QuickBird fractions.

5. Conclusions

This study demonstrated the application of a tool developed by the authors for spectral mixture analysis (SMA) that helps determine the optimum bands and endmember combinations to produce the minimum RMS and best abundance percentage. The area of study was located in central Greater Cairo, and the imagery data used in this study was Hyperion data (EO-1) with a spatial resolution of 30 m from a 705-km orbit. Atmospheric correction (FLAASH) and geometric correction techniques were applied to the imagery data.

A set of all available combinations of endmembers were calculated using the developed tool. In each combination, suitable bands were selected according to a predefined separability distance (8.5%). Increasing the separability distance enhanced the band selection and helped in distinguishing different material within a single pixel. The selected bands were used to calculate abundance fractions and associated RMSE values. The last function of the tool was to assess all the abundances percentages and RMS values resulting from running SMA iteratively using the available combinations on a pixel-by-pixel basis, and then to come up with the best combination of endmembers that produce the minimum RMS and best abundance percentages.

The tool was developed using ENVI/IDL and Python scripting language, and it is encapsulated as a tool that can be used directly from ESRI ArcGIS.

Future studies require focusing on automating the intelligence selection of endmembers that could logically fit with each other e.g., High Albedo and Low Albedo or Shallow Water and Sabkha. However, in this study, all the available combinations were calculated regardless of the correlation of existence among endmembers within the same combination. Another aspect of development based on this study would be to design a comprehensive GIS Data-Model that accommodates the combination attributes (endmember names, CID, land-use type) and establish a relation with the three output raster images (Suitability Model, Abundance Percentage Values, RMS Values). This relation would facilitates information retrieval for each pixel in the image and help the generation of LandUse maps.

References

- Adams, J.B., Smith, M.O., & Gillespie, A.R. (1993). Imaging Spectroscopy: Interpretation based on Spectral Mixture Analysis. In C.M. Pieters & P. Englert (Eds.), *Remote Geochemical Analysis: Elemental and Mineralogical Composition* (pp. 145–166). Cambridge: Cambridge University Press.
- Adams, J.B., Smith, M.O., & Johnston, P.E. (1986). Spectral Mixture Modeling: A New Analysis of Rock and Soil Types at the Viking Lander Site. *Journal of Geophysical Research*, 91.
- Adams, J.B., Sobol, D.E., Kapos, V., Filho, R.A., Roberts, D.A., Smith, M.O., & Gillespie, A.R. (1995). Classification of Multispectral Images Bases on Fractions of Endmembers: Application to Land-Cover Change in the Brazilian Amazon. *Remote Sensing of Environment*, 52, 137–154.
- Beck, R. (2003). EO-1 User Guide, Version 2.3. In. Cincinnati, Ohio: Prepared for Satellite Systems Branch USGS Earth Resources Observation Systems Data Center (EDC).
- Boardman, J.W., Kruse, F.A., & Green, R.O. (1995). Mapping Target Signatures via Partial Unmixing of AVIRIS Data. *Summaries, Fifth JPL Airborne Earth Science Workshop*, JPL Publications 95-1, 1, 23–26.
- Campbell, J.B., & Wynne, R.H. (2011). *Introduction to Remote Sensing*. (5th ed.). New York: The Guilford Press.
- Chen, C.M., Hepner, G.F., & Forster, R.R. (2003). Fusion of Hyperspectral and Radar Data using the IHS Transformation to Enhance Urban Surface Features. *ISPRS Journal of Photogrammetry & Remote Sensing*, 58, 19–30.
- Chen, X., & Vierling, L. (2006). Spectral mixture analyses of hyperspectral data acquired using a tethered balloon. *Remote Sensing of Environment*, 103, 338–350.
- Franke, J., Roberts, D.A., Halligan, K., & Menz, G. (2009). Hierarchical Multiple Endmember Spectral Mixture Analysis (MESMA) of hyperspectral imagery for urban environments. *Remote Sensing of Environment*, 113, 1712–1723.
- Fugate, D. (2003). *Urban Health in Environmental Context: The Application of Remote Sensing and GIS to a Case Study in Cairo, Egypt*. In Department of Geography. San Diego: San Diego State University.
- Fugate, D., Tarnavsky, E., & Stow, D. (2010). A Survey of the Evolution of Remote Sensing Imaging Systems and Urban Remote Sensing Applications. In T. Rashed & C. Juergens (Eds.), *Remote sensing of urban and suburban areas* (pp. 119–139). Dordrecht ; London: Springer.
- Guo, L., Chehata, N., Mallet, C., & Boukir, S. (2011). Relevance of airborne lidar and multispectral image data for urban scene classification using Random Forests *ISPRS Journal of Photogrammetry and Remote Sensing*, 66, 56–66.
- Herold, M., Gardenr, M.E., & Roberts, D.A. (2003). Spectral Resolution Requirements for Mapping Urban Areas. *IEEE Transactions on Geosciences and Remote Sensing*, 41, 1907–1919.
- Herold, M., Roberts, D.A., Gardner, M.E., & Dennison, P.E. (2004). Spectrometry for urban area remote sensing—Development and analysis of a spectral library from 350 to 2400 nm. *Remote Sensing of Environment*, 91, 304–319.
- Herold, M., Roberts, D.A., Noronha, V., & Smadi, O. (2008). Imaging spectrometry and asphalt road surveys. *16, Transportation Research C*, 153–166.
- Mesev, V. (2003). *Remotely sensed cities*. London ; New York: Taylor & Francis.
- Milton, E.J. (1999). Image Endmembers and the Scene Model. *Canadian Journal of Remote Sensing*, 25, 112–120.
- NRC (2007). *Earth science and applications from space: National imperatives for the next decade*. In. Washington, D.C.: National Research Council.
- Pearlman, J., Carman, S., Segal, C., Jarecke, P., Clancy, P., & Browne, W. (2000). Overview of the Hyperion Imaging Spectrometer for the NASA EO-1 mission In, *Geoscience and Remote Sensing Symposium, 2001. IGARSS '01. IEEE 2001 International* (pp. 3036–3038): IEEE Conference Publications.
- Pignatti, S., Cavalli, R.M., Cuomo, V., Fusilli, L., Pascucci, S., Poscolieri, M., & Santini, F. (2009). Evaluating Hyperion capability for land cover mapping in a fragmented ecosystem: Pollino National Park, Italy. *Remote Sensing of Environment*, 113, 622–634.

- Plaza, A., Benediktsson, J.A., Boardman, J.W., Brazile, J., Bruzzone, L., Camps-Valls, G., Chanussot, J., Fauvel, M., Gamba, P., Gualtieri, A., Marconcini, M., Tilton, J.C., & Triann, G. (2009). Recent advances in techniques for hyperspectral image processing. *Remote Sensing of Environment*, 113.
- Powell, R.L., & Roberts, D.A. (2008). Characterizing variability of the urban physical environment for a suite of cities in Rondônia, Brazil. *Earth Interactions*, 12, 1–32.
- Powell, R.L.R., D. A., Dennison, P.E., & Hess, L.L. (2007). Sub-pixel mapping of urban land cover using multiple endmember spectral mixture analysis: Manaus, Brazil. *Remote Sensing of Environment*, 106, 253–267.
- Rashed, T. (2008). Remote Sensing of Within-Class Changes in Urban Neighborhood Structures. *Computer, Environment and Urban Systems*, 32, 343–354.
- Rashed, T., & Juergens, C. (2010). Remote sensing of urban and suburban areas. In *Remote sensing and digital image processing v 10*. Dordrecht ; London: Springer.
- Rashed, T., Weeks, J., Gadalla, M., & Hill, A. (2001). Revealing the Anatomy of Cities through Spectral Mixture Analysis of Multispectral Satellite Imagery: A Case Study of the Greater Cairo Region, Egypt. *Geocarto International*, 16, 5–16.
- Rashed, T., Weeks, J., Roberts, D.A., Rogan, J., & Powell, P. (2003). Measuring the Physical Composition of Urban Morphology using Multiple Endmember Spectral Mixture Models. *Photogrammetric Engineering & Remote Sensing*, 69, 1011–1020.
- Rashed, T., Weeks, J., Stow, D., & Fugate, D. (2005). Measuring Temporal Compositions of Urban Morphology through Spectral Mixture Analysis: Toward a Soft Approach to Change Analysis in Crowded Cities. *International Journal of Remote Sensing*, 26, 699–718.
- Roberts, D.A., Batista, G.T., Pereira, J.L.G., Waller, E.K., & Nelson, B.W. (1998a). Change Identification Using Multitemporal Spectral Mixture Analysis: Applications in Eastern Amazonia. In R.S. Lunetta & C.D. Elvidge (Eds.), *Remote Sensing Change Detection: Environmental Monitoring Applications and Methods* (pp. 137–161). Ann Arbor, MI: Ann Arbor Press.
- Roberts, D.A., Gardner, M., Church, R., Ustin, S., Scheer, G., & Green, R.O. (1998b). Mapping Chaparral in the Santa Monica Mountains using Multiple Endmember Spectral Mixture Model. *Remote Sensing of Environment*, 65, 267–279.
- Roberts, D.A., Quattrochi, D.A., Hulley, G.C., Hook, S.J., & Green, R.O. (2012). Synergies between VSWIR and TIR data for the urban environment: An evaluation of the potential for the Hyperspectral Infrared Imager (HyspIRI) Decadal Survey mission. *Remote Sensing of Environment*, 117, 83–101.
- Rogge, D.M., Rivard, B., Zhang, J., Sanchez, A., Harris, J., & a, J.F. (2007). Integration of spatial–spectral information for the improved extraction of endmembers. *Remote Sensing of Environment*, 110, 287–303.
- Small, C. (2001). Estimation of Urban Vegetation Abundance by Spectral Mixture Analysis. *International Journal of Remote Sensing*, 22, 1305–1334.
- Somers, B., Delalieux, K.C.S., Stuckens, J., Zande, D.V.d., Verstraeten, W.W., & Coppin, P. (2009). Nonlinear Hyperspectral Mixture Analysis for tree cover estimates in orchards. *Remote Sensing of Environment*, 113, 1183–1193.
- Sutton, K., & Fahmi, W. (2001). Cairo's Urban Growth Master Plans in the Light of Egypt's 1996 Population Census Results. *Cities, The International Journal of Urban Policy and Planning*, 18, 135–149.
- Tompkins, S., Mustard, J.F., Pieters, C.M., & Forsyth, D.W. (1997). Optimization of Endmembers for Spectral Mixture Analysis. *Remote Sensing of Environment*, 59, 472–489.
- Weeks, J., Getis, A., Hill, A., Rashed, T., & Gadalla, M. (2004). The Fertility Transition in Egypt: Intra-Urban Patterns in Cairo. *Annals of the Association of American Geographers*, 94, 74–93.
- Weng, Q. (2008). Remote sensing of impervious surfaces. In *Taylor & Francis series in remote sensing applications* (pp. xxvii, 454). Boca Raton: CRC Press.
- Weng, Q. (2012). Remote sensing of impervious surfaces in the urban areas: Requirements, methods, and trends. *Remote Sensing of Environment*, 117, 34–49.

Weng, Q., & Quattrochi, D.A. (2007). Urban remote sensing. Boca Raton: CRC Press.

Weng, Q., Quattrochi, D.A., & Carlson, T.N. (2012). Remote sensing of urban environments: Special issue. Remote Sensing of Environment, 117, 1–2.

Wu, C., & Murray, A.T. (2003). Estimating Impervious Surface Distribution by Spectral Mixture Analysis. Remote Sensing of Environment, 84.

Waleed Effat is a GIS Technical Consultant at ESRI Northeast Africa, Egypt since 2005. He is a Ph.D. student at the Faculty of Computers and Information, Cairo University, Egypt from 2010 till the present. His major fields of study are geographical information systems and remote sensing.

Osman Mohamed Hegazy is Professor of Information (Data Engineering) since 1992 at Information Systems, Cairo University, Egypt. He has a Bachelor degree in Electronic Engineering, Faculty of Engineering, Cairo University, Egypt, 1964; Ph.D. in Computer Engineering, University of Leicester, England, 1977. His major fields of study are data engineering, cloud computing and the computer/ human interface.

Mohamed NourEldien is an Associate Professor at Information Systems, Faculty of Computers and Information, Cairo University, Egypt since 2002. He has a Ph.D. in GIS and Information systems from Louis Pasteur University, France, 2001. His major fields of study are geographical information systems, data mining, ecommerce and e-business.

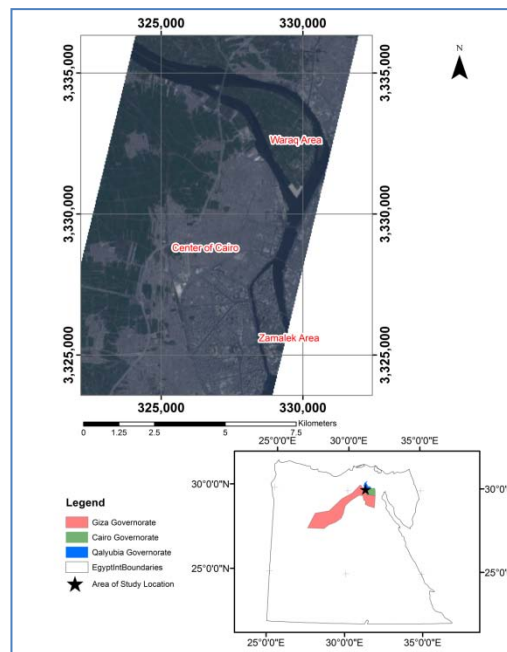


Figure 1: Hyperion image of the area of study and its location with respect to Egypt's international boundaries.

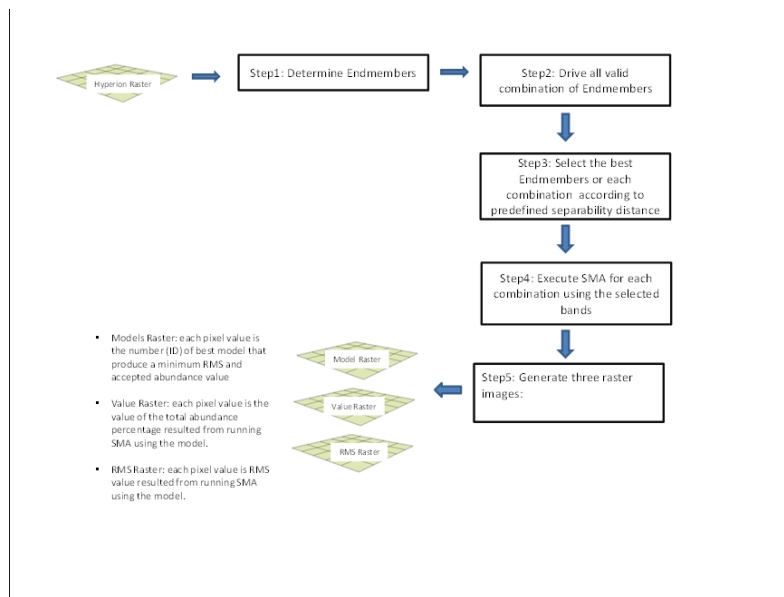


Figure 1: Main elements of the Multiband MESMA approach (conceptual model of algorithm)

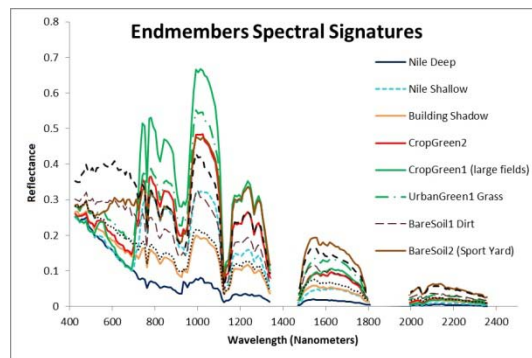


Figure 2: Derived endmembers for the area of study.

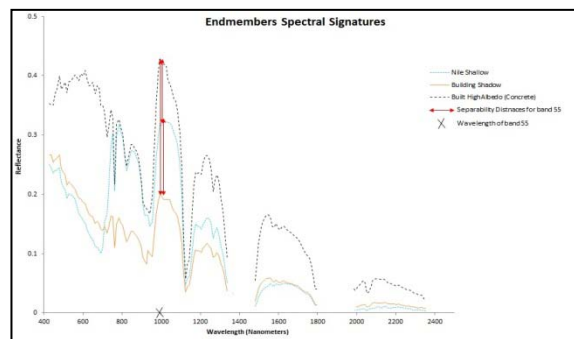


Figure 3: Separability distance for bands 55 and 59.

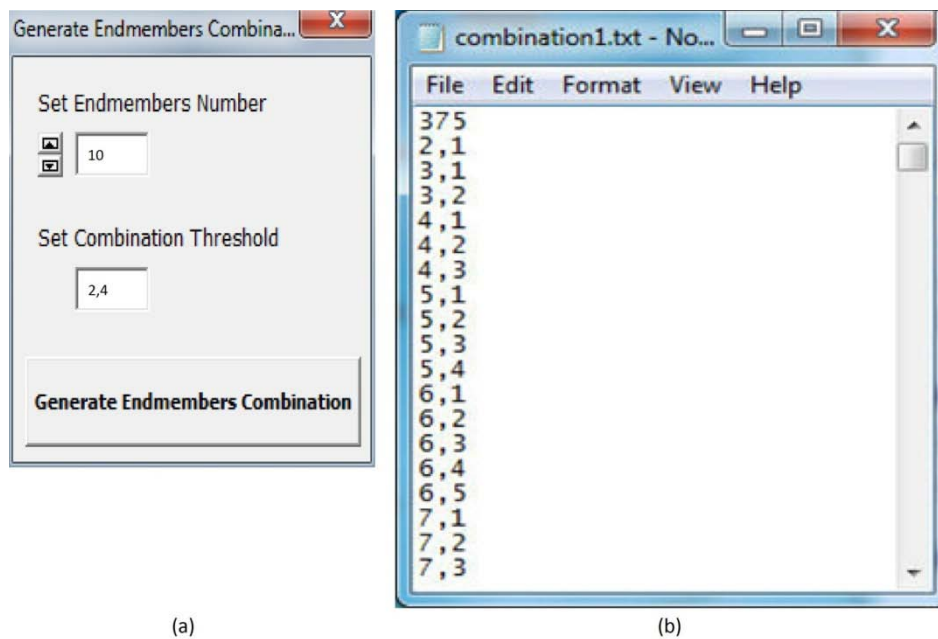


Figure 5: (a) Developed widget by which all possible endmember combinations on a per-pixel basis are created. (b) Output text file that contains total number of available combinations of the provided endmembers, in addition to listing each combination and the endmembers used in that combination.

```
File Edit Format View Help
1102 Built_HighAlbedo_Concerte,BuildingShadow,Nile_Deep 31,32,34,35,36,37,41,42,43,44,45,54,
1103 Built_HighAlbedo_Concerte,BuildingShadow,Nile-Shallow 54,55,56,57,58,59
1107 Built_HighAlbedo_Concerte,CropGreen1_large_fields,Nile_Deep 28,30,31,32,33,34,35,36,37,
1108 Built_HighAlbedo_Concerte,CropGreen1_large_fields,Nile-Shallow 28,30,54,55,56,57,58,59,
1109 Built_HighAlbedo_Concerte,CropGreen1_large_fields,BuildingShadow 28,30,31,32,33,34,35,3
1111 Built_HighAlbedo_Concerte,UrbanGreen1_Grass,Nile_Deep 11,12,13,14,15,16,17,18,19,20,21,
1112 Built_HighAlbedo_Concerte,UrbanGreen1_Grass,Nile-Shallow 13,14,15,16,17,18,19,20,21,22,
1113 Built_HighAlbedo_Concerte,UrbanGreen1_Grass,BuildingShadow 28,53,54,55,56,57,58,59,60,6
1115 Built_HighAlbedo_Concerte,UrbanGreen1_Grass,CropGreen1_large_fields 20,22,23,24,25,26,5
1116 Built_HighAlbedo_Concerte,BareSoil1_Dirt,Nile_Deep 7,8,9,10,11,12,13,14,15,16,17,18,19,
1117 Built_HighAlbedo_Concerte,BareSoil1_Dirt,Nile-Shallow 5,6,7,8,9,10,11,12,13,14,15,16,17
1118 Built_HighAlbedo_Concerte,BareSoil1_Dirt,BuildingShadow 11,12,13,14,15,16,17,18,19,20,2
1119 Built_HighAlbedo_Concerte,BareSoil1_Dirt,CropGreen2 15,16,17,18,19,20,21,22,23,24,25,26
1120 Built_HighAlbedo_Concerte,BareSoil1_Dirt,CropGreen1_large_fields 5,6,7,8,9,14,15,16,17,
1121 Built_HighAlbedo_Concerte,BareSoil1_Dirt,UrbanGreen1_Grass 21,22,23,24,25,54,55,56,57,5
1122 Built_HighAlbedo_Concerte,BareSoil1_SportYard,Nile_Deep 12,13,14,15,16,17,18,19,20,21,22
1123 Built_HighAlbedo_Concerte,BareSoil1_SportYard,Nile-Shallow 13,14,15,16,17,18,19,20,21,22
1124 Built_HighAlbedo_Concerte,BareSoil1_SportYard,BuildingShadow 15,16,17,18,19,20,21,22,23,
1125 Built_HighAlbedo_Concerte,BareSoil1_SportYard,CropGreen2 16,17,18,19,20,21,22,23,24,25
1126 Built_HighAlbedo_Concerte,BareSoil1_SportYard,CropGreen1_large_fields 15,16,17,18,19,20,
1127 Built_HighAlbedo_Concerte,BareSoil1_SportYard,UrbanGreen1_Grass 19,20,21,22,23,24,25
1128 Built_HighAlbedo_Concerte,BareSoil1_SportYard,BareSoil1_Dirt 60,61,62,63
```

Figure 6: Output text file showing endmembers and band combinations

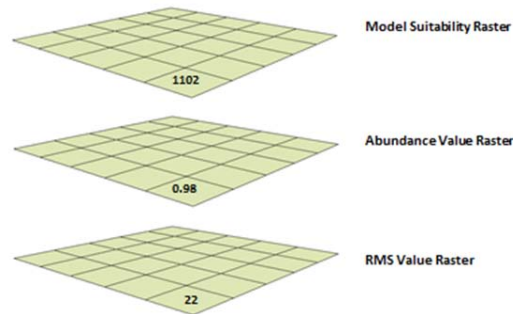


Figure 7: Three output raster images generated from the developed algorithm



Figure 8: Sample from selected ground control points (red crosses)

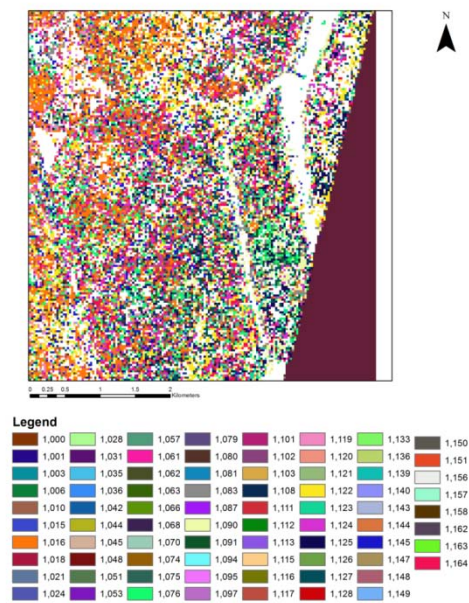


Figure 9: Output suitability model raster generated from an algorithm, in which each pixel value contains the combination ID that gives the best RMSE and abundance values

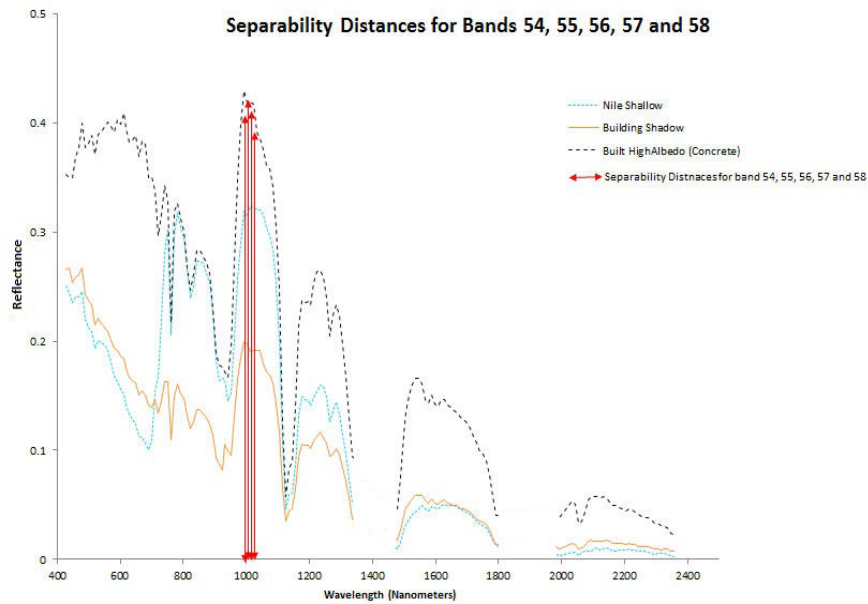


Figure 10: Separability distances for bands 54, 55, 56, 57, and 58

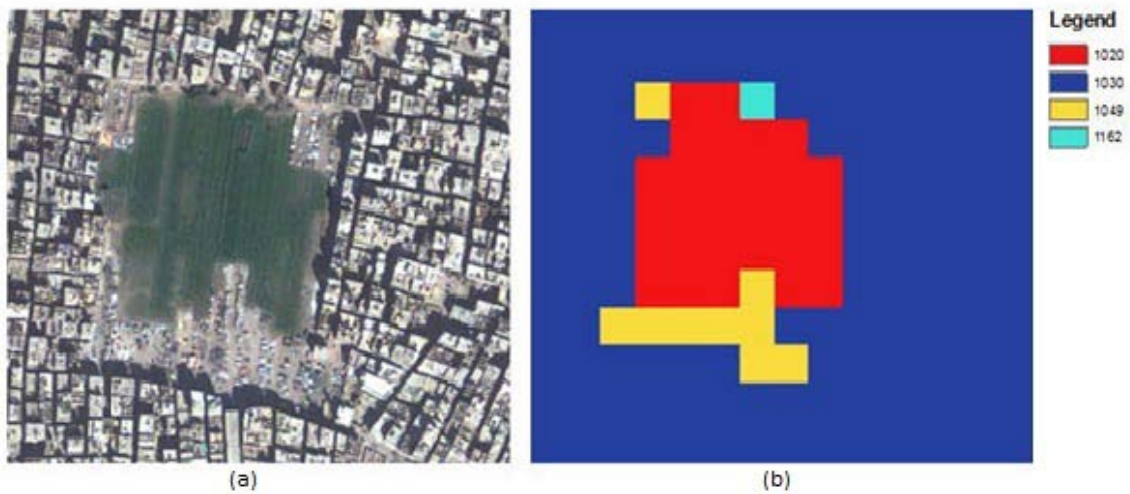


Figure 11: (a) High-resolution image (QuickBird). (b) Suitability Model Raster for the same area.

Model 1020 consists of BareSoil1_Dirt and UrbanGreen1Grass endmembers

Model 1030 consists of Building Shadow, Built LowAlbedo and Built HighAlbedo endmembers

Model 1049 consists of Building Shadow and Built LowAlbedo endmembers

Model 1162 consists of Built LowAlbedo and BareSoil1 Dirt endmembers

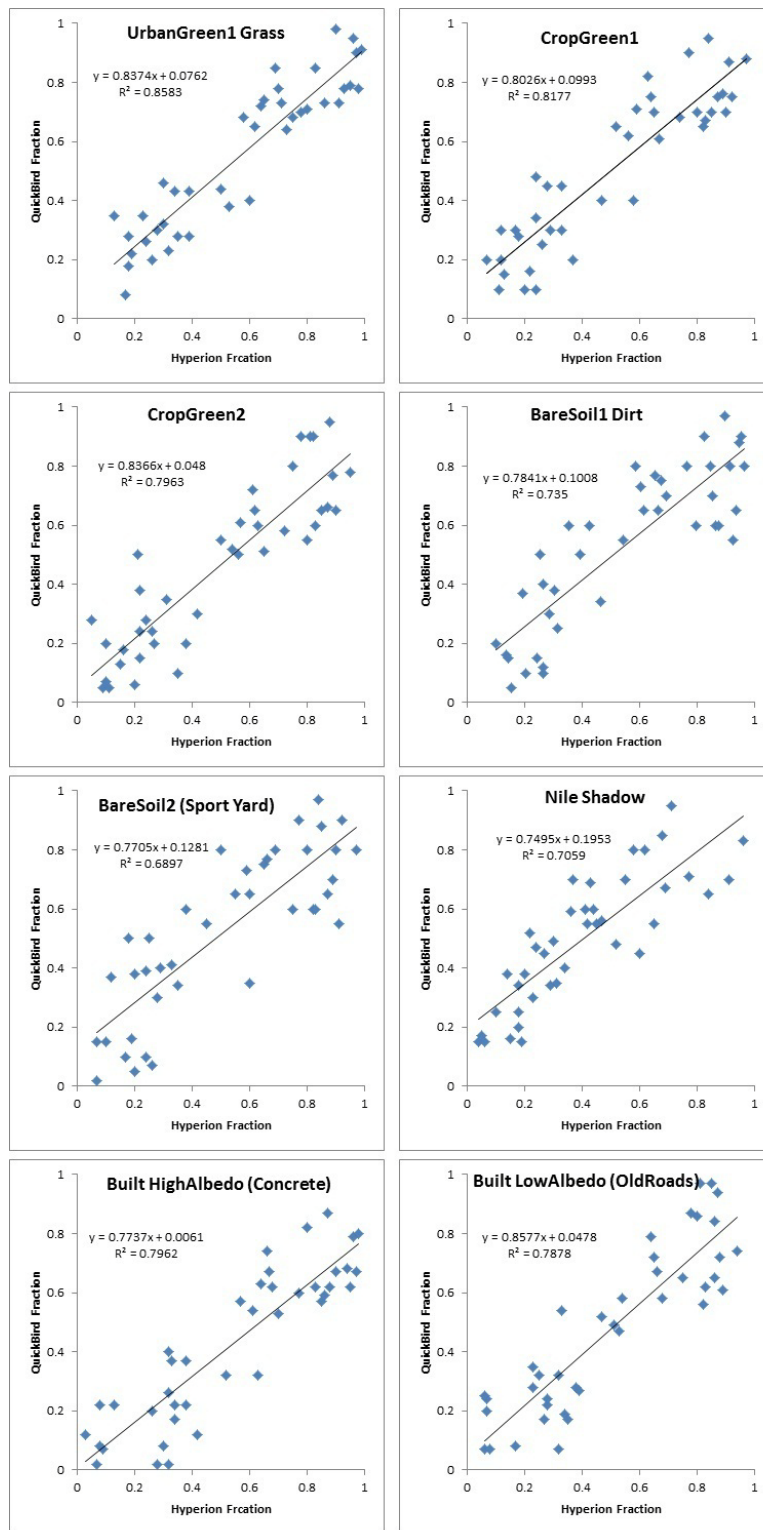


Figure 12: Regression line between Hyperion fractions and QuickBird fractions for each generalized endmember.

Table 1. List of Extracted Endmembers

Index	Endmember Name	Description
1	Nile Deep	The deep area in the Nile River
2	Nile Shallow	The shallow area in the Nile River
3	Building Shadow	The shadow of the buildings within the area of the study
4	CropGreen2	Medium sized crop fields mainly including some vegetables crops
5	CropGreen1 (large fields)	Large sized crop fields mainly including wheat and cotton crops
6	UrbanGreen1 Grass	Green areas within residential areas (parks)
7	BareSoil1 Dirt	Lands that is ready to be cultivated with no vegetation.
8	BareSoil2 (Sport Yard)	Sport yard areas
9	Built HighAlbedo (Concrete)	Concrete structures and newly paved roads
10	Built LowAlbedo (OldRoads)	Old roads

This table lists the extracted endmembers and provides a full description for each endmember.

Table 2. Summary of endmember combination models, endmembers for each combination and number of bands.

Number of Combination	Number of used Endmembers
45	2
120	3
210	4

This table lists the endmember combination models, endmembers for each combination and number of bands.

Table 3. Content of one row of output textfile

Combination ID	Endmembers	Band Index
1103	Built_HighAlbedo_Concrete, BuildingShadow, Nile-	54,55,56,57,58

This table lists the content of one row in the output textfile.

Table 1. Band wavelength values

Band index	Wavelength (Nanometers)
54	972.993408
55	983.081665
56	993.17041
57	1003.299377
58	1013.298218

This tables list lists the wavelengths for each band listed in Table 3, and are plotted in a graph as shown in Figure (10)

Table 5. Regression outputs: Slope, interception, and R2 values for each endmember

Endmember	Slope	Interception	R2
UrbanGreen1 Grass	0.837	7.6%	0.858
CropGreen1	0.803	9.9%	0.818
CropGreen2	0.837	4.8%	0.796
BareSoil1 Dirt	0.784	10%	0.735
BareSoil2 (Sport Yard)	0.771	12.8%	0.69
Nile Shadow	0.75	19.5%	0.706
Built_HighAlbedo (Concrete	0.774	0.6%	0.797
Built_LowAlbedo (OldRoads)	0.858	4.78%	0.78

This table illustrates the slope, interception, and R^2 values for each endmember.

This academic article was published by The International Institute for Science, Technology and Education (IISTE). The IISTE is a pioneer in the Open Access Publishing service based in the U.S. and Europe. The aim of the institute is Accelerating Global Knowledge Sharing.

More information about the publisher can be found in the IISTE's homepage:

<http://www.iiste.org>

CALL FOR PAPERS

The IISTE is currently hosting more than 30 peer-reviewed academic journals and collaborating with academic institutions around the world. There's no deadline for submission. **Prospective authors of IISTE journals can find the submission instruction on the following page:** <http://www.iiste.org/Journals/>

The IISTE editorial team promises to review and publish all the qualified submissions in a **fast** manner. All the journals articles are available online to the readers all over the world without financial, legal, or technical barriers other than those inseparable from gaining access to the internet itself. Printed version of the journals is also available upon request of readers and authors.

IISTE Knowledge Sharing Partners

EBSCO, Index Copernicus, Ulrich's Periodicals Directory, JournalTOCS, PKP Open Archives Harvester, Bielefeld Academic Search Engine, Elektronische Zeitschriftenbibliothek EZB, Open J-Gate, OCLC WorldCat, Universe Digital Library, NewJour, Google Scholar

